Supplementary Information & Methods

Cristae formation is a mechanical buckling event controlled by the inner membrane lipidome

Kailash Venkatraman, Christopher T. Lee, Guadalupe C. Garcia, Arijit Mahapatra, Guy Perkins, Keun-Young Kim, H. Amalia Pasolli, Sebastien Phan, Jennifer Lippincott-Schwartz, Mark Ellisman, Padmini Rangamani, and Itay Budin

Contents:

Supplementary Figures

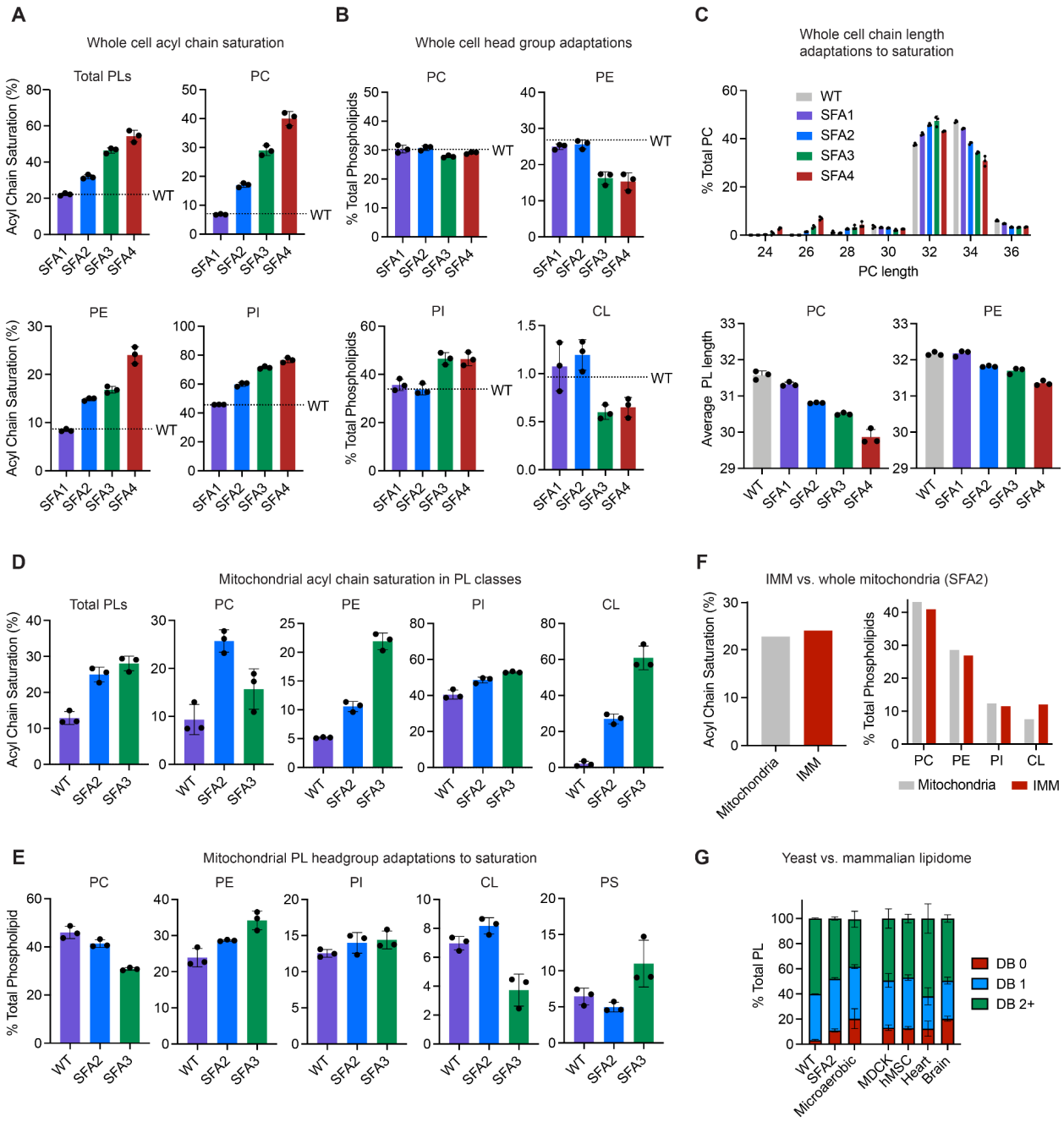

Figure S1: Changes to whole cell and mitochondrial lipid profile upon modulation of Ole1p expression.

(A) Decreasing Ole1p expression increases the acyl chain saturation of the total yeast PL pool, and major PL classes as assayed by lipidomics, error bars indicate SD, n=3 independent cultures. WT levels are shown as dotted lines.

(B) Potentially compensatory changes to the whole cell lipidome in response to increasing saturation. Shown are the abundance of major yeast PLs in SFA strains, n=3 independent cultures. WT levels shown as dotted lines. As saturation increases, PE and CL decrease, while PI increases. Error bars indicate SD.

(C) Increasing lipid saturation results in shortening of PC and PE acyl chains in the whole cell. Shown are the sum of the lengths for the *sn*-1 and *sn*-2 chains.
(D) Acyl chain saturation in isolated mitochondria from SFA strains and WT as determined by intact lipid analysis for the total PL pool, n=3 independent cultures. Error bars indicate SD.
(E) PL headgroup adaptations in isolated mitochondria from SFA strains and wild-type in major PL classes as determined by lipidomic analysis, n=3 independent cultures. In the mitochondria, PC decreases and PE increases as saturation increases. Error bars indicate SD.
(F) The IMM and whole mitochondrial lipidome display similar levels of saturation and PE/PC, but differ in abundance of CL (higher in the IMM).
(G) Mammalian lipidomes contain similar lipid saturation profiles to yeast SFA2 and micro-aerobically grown cells, where CL is essential. Shown is the double bond profile of all PLs as determined through lipidomics from *S. cerevisiae* (this study) in comparison with mammalian cell lines (MDCK-CM and hMSC-CM) and isolated tissues previously analyzed using the same lipidomics platform[140]. WT yeast grown under vigorous aeration have a low number of saturated and monounsaturated PLs, while WT cells grown under physiologically-relevant oxygen concentrations (microaerobic) or engineered strains (SFA2) show profiles more similar to mammalian cells. In the latter systems, CL is an essential component for proper mitochondrial biogenesis. Error bars indicate SD.

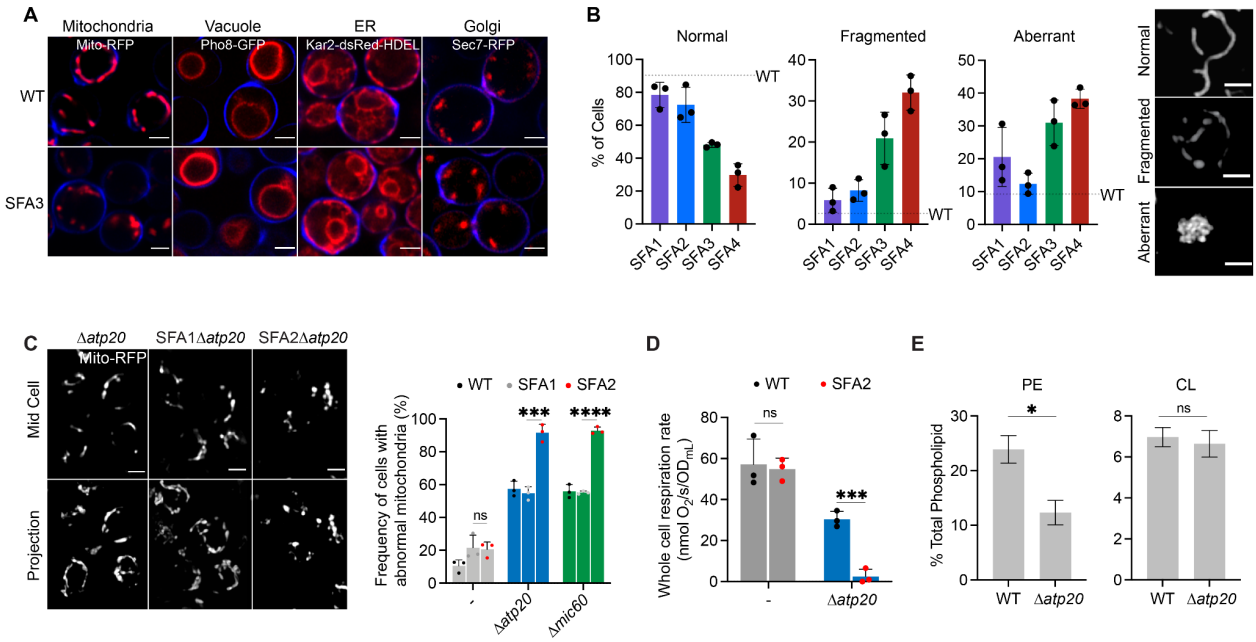

Figure S2: Effects of PL saturation on organelle morphology and its interactions with cristae shaping proteins.

(A) Decreasing expression of Ole1p expression results in abnormal mitochondria in SFA3 while other organelles remain intact. Organelles were imaged in cells that were transformed with plasmids expressing the following fusion proteins: mts-RFP (Mitochondria), Pho8-GFP (Vacuole), Kar2-dsRed-HDEL (ER), Sec7-RFP (Golgi). Cells were grown to exponential phase and were stained with cell wall-binding calcofluor white (blue). Scale bars, 2 μm.

(B) Imaging of matrix-localized mito-RFP was used to quantify the frequency of mitochondrial abnormality as a function of the amounts of normal, fragmented and aberrant mitochondria. Normal mitochondria contain tubulations throughout the whole yeast cell, while fragmented mitochondria retain an overall mitochondrial structure but have lost the interconnected tubular network associated with normal mitochondria. Aberrant mitochondria are characterized by punctate aggregations of mitochondria in the center of the yeast cell. Cells were imaged in n=3 independent cultures. Error bars indicate SD. Scale bars, 2 μm.

(C) Representative Airyscan confocal micrographs of yeast expressing matrix-localized RFP (mts-RFP). (Right) Frequency of mitochondrial abnormalities as assayed by analysis of mts-RFP. N>50 cells were counted in biological triplicate (n=3) in each condition. Error bars indicate SD. ***p=0.0006, ****p <0.0001 unpaired two-tailed t-test compared SFA2Δ*atp20* and SFA2Δ*mic60* against SFA1Δ*atp20* and SFA1Δ*mic60* respectively.

(D) Respiration rates in Δ*atp20* and SFA2Δ*atp20* cells measured in biological triplicate (n=3) using a Clark electrode. Error bars represent SD. ***p < 0.0005, unpaired two-tailed t-test compared against Δ*atp20*.

(E) Lipidomics on isolated Δ*atp20* mitochondria reveals decreased levels of PE while the levels of CL remain the same. Error bars indicate SD.

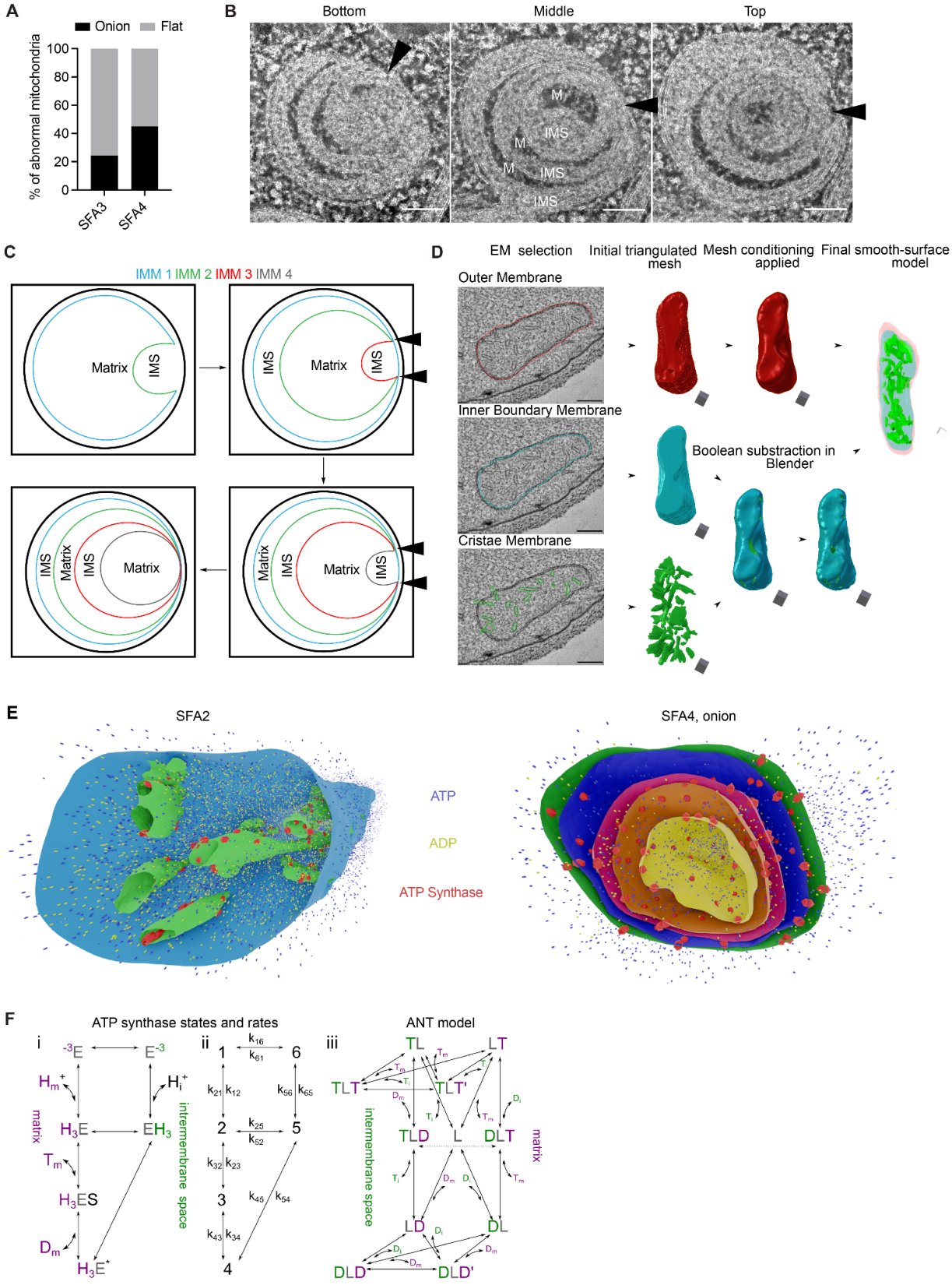

Figure S3: Multi-tilt tomography and analysis of subsequent reconstructions reveals a potential mechanism for loss of ATP production in onion-like mitochondria.

(A) Quantitative analysis of thin-section TEM micrographs reveals the abnormal mitochondria in SFA3 are predominantly flat, while in SFA4 there is an even distribution of onion and flat abnormal mitochondria. At least N=40 mitochondria were quantified from each strain.
(B) Multi-tilt tomogram slices of HPFS SFA4 yeast cells at three z-positions. 'M' indicates matrix regions (dark), while 'IMS' indicates intermembrane space regions (light). Shading indicates alternating matrix and IMS regions, as previously observed[19]. Black triangles indicate observed regions of contact points between IMM layers, suggesting a continuous IMM. Scale bars, 100 nm.
(C) Schematic depiction for one model of how onion-like morphology could be formed by a continuous IMM undergoing subsequent buddings. Black triangles indicate regions of contact points between multiple apparent IMM layers.
(D) Example of Blender-based 3D Mesh generation pipeline from EM tomograms.
(E) Snapshots of ATP generation simulations as displayed in Movie S4 and S5. SFA2 shows localizations of ATP synthases to regions of high curvature in CMs, while in the SFA4 onion ATP synthases are distributed evenly on each layer of IMM based on previous cryo electron tomography reconstructions.
(F) (i-iii) Schematic representations of the kinetic states and modeled rates of ATP synthase and ANT used to construct the metabolic model. Further details of the model can be found in the Supplementary Text.

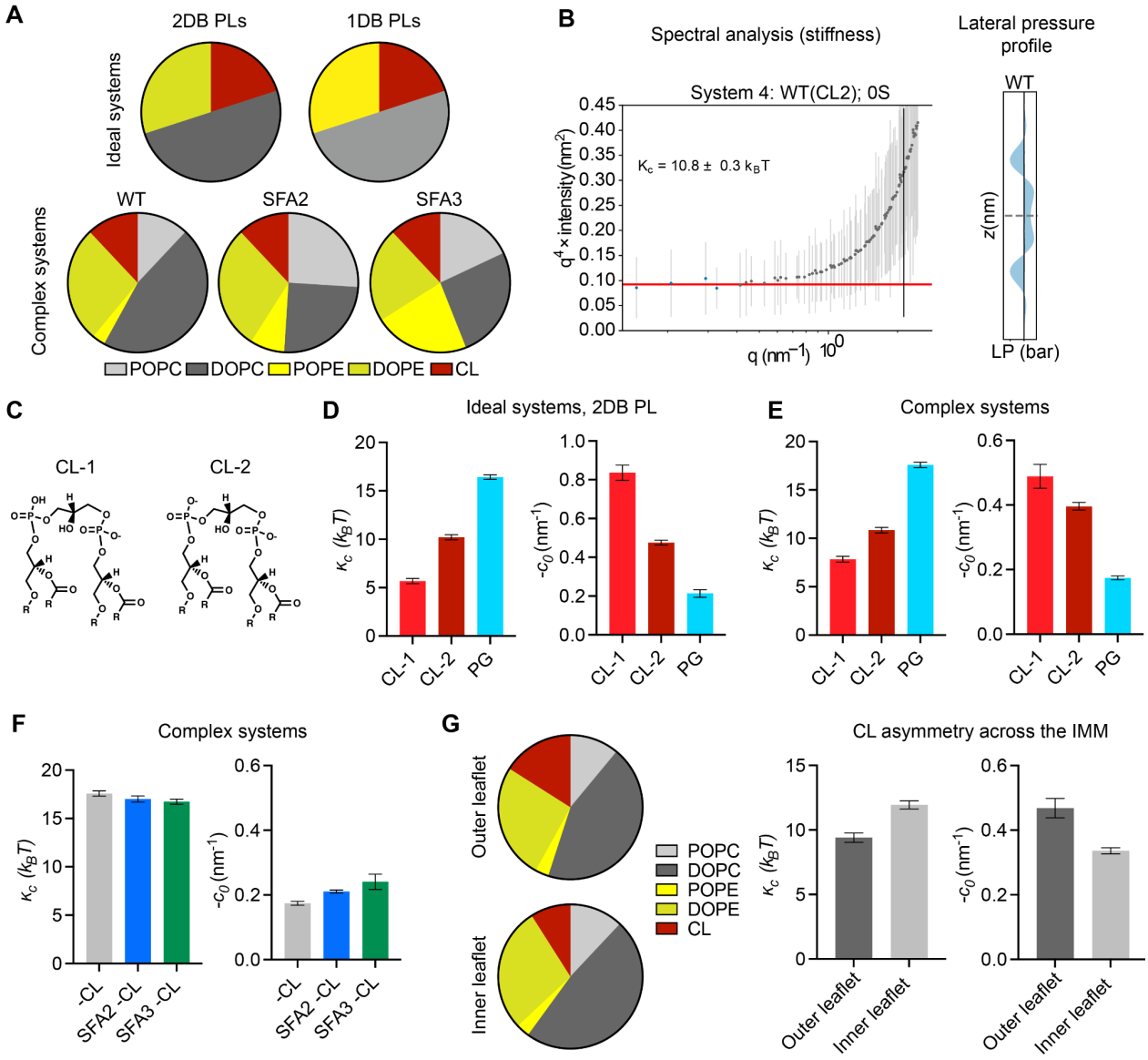

Figure S4: Coarse-grained molecular dynamics predicts an important role for CL in shaping membrane mechanical properties.

(A) Ideal systems contained lipid compositions of fixed abundance, while changing the unsaturation of the acyl chains from di-unsaturated to monounsaturated. In contrast, the 'complex' systems mimicking the mitochondrial lipidomes of SFA strains accounted for headgroup adaptations to increasing saturation, such as increasing PE. Full compositions are listed in Table S2.

(B) Example spectral analysis of thermal undulations, used to calculate bending moduli, and lateral pressure profiles, used to calculate spontaneous curvature.

(C) Chemical structures of CL in dianion (CL-2) and monoanion (CL-1) ionization states.

(D) In ideal systems, the changing of ionization state of CL from -1 to -2 causes a minor increase in membrane stiffness and a major reduction in spontaneous curvature. Absence of CL increases membrane stiffness and reduces spontaneous curvature as determined through MARTINI CG-MD.

(E) Accounting for headgroup adaptations in complex systems, simulations still show the same trend with dianionic CL and loss of CL showing increases in membrane stiffness and a reduction in spontaneous curvature.
(F) While increasing lipid saturation has a minimal effect on membrane stiffness in the absence of CL, the increase in the magnitude of spontaneous curvature suggests that the presence of PE can partially, but not completely, compensate for loss of curvature provided by CL.
(G) Modeling of outer leaflet enrichment of CL in the yeast IMM. Simulated changes in CL concentrations reported in Gallet et. al[102] results in membrane softening and increased spontaneous curvature. Two sets of simulations were set up with the estimated compositions of the outer and inner IMM leaflets shown in the pie charts. The simulated outer membrane systems were softer (lower stiffness) and had a larger negative spontaneous curvature. The difference in the outer and inner leaflet curvatures was 0.1±0.04 nm^{-1}, which is an estimation for asymmetry-induced c_0.

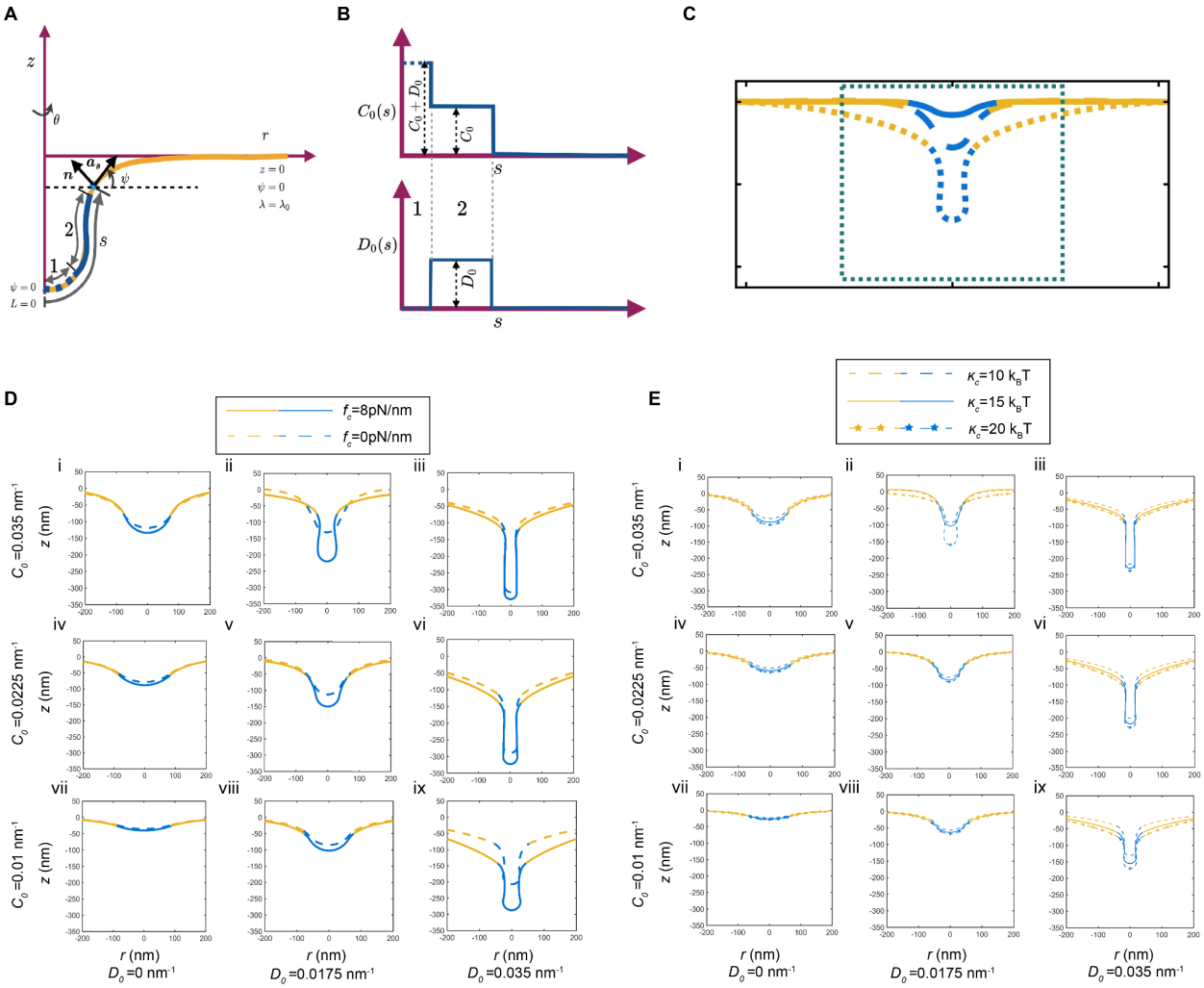

Figure S5: Continuum modeling details and comparison of tubular morphologies with and without an applied collar force.

(A) Schematic showing the axisymmetric membrane configuration along with the boundary conditions. The yellow regions depict the bare lipid bilayer, and the blue regions depict the regions where different spontaneous curvatures are prescribed.

(B) Prescription of isotropic and anisotropic spontaneous curvature along the arc length in the simulations.

(C) The simulation domain is large to avoid boundary effects but the zoomed in portion in the dashed box is shown to demonstrate the shapes of the membrane.

(D) Comparison of the tubular shapes with (solid lines) and without (dashed line) the collar force at the base of the cristae. All parameters are the same as those in Figure 5B. Presence of a collar force promoted cristae like structures for the same values of imposed curvatures. This is particularly apparent in panel ii.

(E) Shapes of the membrane for the same values of coat area, collar force, and variations in the isotropic and anisotropic spontaneous curvature as panel D for different values of bending modulus. We observe that the shapes of the tubular cristae are not sensitive to changes in bending modulus for low curvature values but differences in membrane curvature can be seen for high values of isotropic and anisotropic spontaneous curvatures.

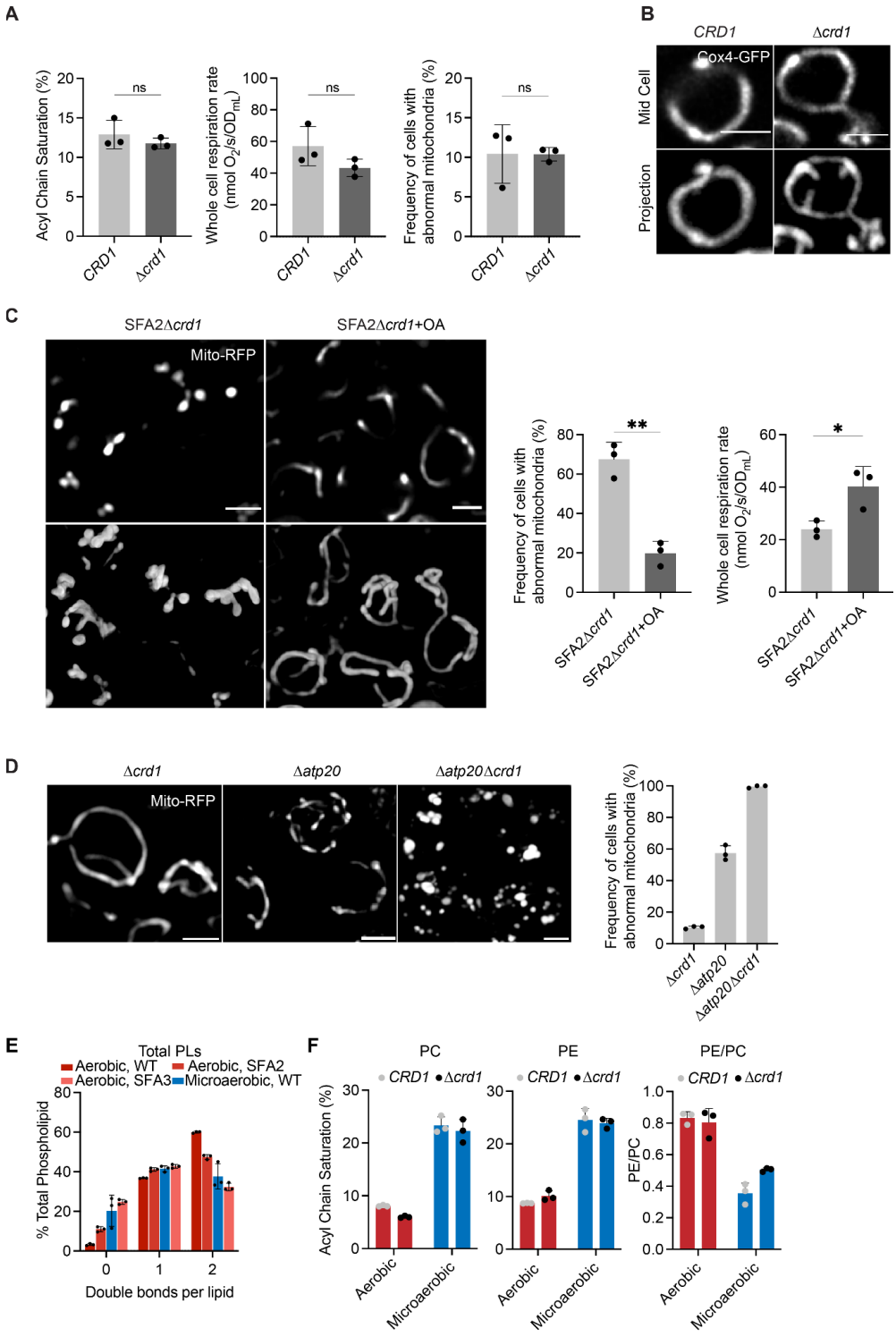

Figure S6: Roles for CL synthesis in shaping mitochondrial morphology.
(A) Mitochondrial PL saturation, respiration rate and mitochondrial abnormality measurements of *CRD1* and Δ*crd1* cells. PL saturation was computed from lipidomics analysis on isolated mitochondria. Respiration measurements were performed using Clark electrode, and mitochondrial abnormalities were determined using confocal microscopy with yeast expressing a

matrix-localized mts-RFP (N>50 cells quantified per replicate). Measurements were taken from independent cultures (n=3), error bars indicate SD.

(B) Airyscan confocal micrographs of aerobic wild-type and Δ*crd1* expressing IMM protein Cox4-GFP. Scale bars, 2 μm. Line profile analysis (below) depicts fluorescent intensity across the indicated mitochondria.

(C) Representative Airyscan confocal micrographs of SFA2Δ*crd1* yeast, grown in the presence and absence of OA, expressing mts-RFP. Scale bars, 2 μm. **p < 0.005, unpaired two-tailed t-test compared against SFA2Δ*crd1*. Respiration rates of SFA2Δ*crd1* cells in the presence and absence of OA were measured in biological replicates (n=3) using a Clark electrode. Error bars indicate SD. *p < 0.05 unpaired two-tailed t-test.

(D) Loss of CL and ATP synthase dimerization results in complete ablation of mitochondrial morphology and structure as assayed by analysis with mts-RFP. N>50 cells were counted in biological triplicate (n=3) in each condition. Error bars indicate SD. Individual deletion of Crd1p results in normal mitochondrial morphology while half of the cells in Δ*atp20* still retain normal morphology. Scale bars, 2 μm.

(E) Lipidomic analysis of the double bond distribution of microaerobic yeast (n=3) shows decreased di-unsaturated PL chains and increased saturated PL chains. This is consistent with an intermediary increase in PL saturation between SFA2 and SFA3 levels. Error bars indicate SD.

(F) The major cellular PL classes, PC and PE, show increased lipid saturation under microaerobic conditions. Also shown is the decrease in whole cell PE/PC ratio under microaerobic conditions, as observed in SFA strains (Figure 3D).

Supplementary Tables

Table S1A: Bending moduli (κ_c) values extracted from X-ray scattering analysis or micropipette aspiration analysis of PC membranes as a function of acyl chain saturation.

X-ray scattering

Lipid	Acyl Chains	κ_c (10^{-20} J)	Source
POPC	16:0 18:1	8.5	[141]
DOPC	18:1 18:1	8.5±0.6	[142]

Micropipette aspiration

Lipid	Acyl Chains	κ_c (10^{-19} J)	Source
SOPC	18:0 18:1	0.90±0.06	[84]
DOPC	18:1 18:1	0.85±0.10	[84]

Table S1B: Bending moduli (κ_c) values extracted from MD simulations of PE as a function of acyl chain saturation.

Lipid	Acyl Chains	κ_c (10^{-20} J)	Source
POPE	16:0 18:1	13.3±0.6	[76]
DOPE	18:1 18:1	11.8±0.3	[76]

Table S1C: Spontaneous curvature (c_0) values extracted from SAXS analysis of PC and PE lipids as a function of acyl chain saturation.

PC

Lipid	Acyl Chains	Matrix	c_0 (nm^{-1})	Source
DPPC	16:0 16:0	DOPE	0.05±0.05	[143]
POPC	16:0 18:1	DOPE	0.01±0.04	[143]
DOPC	18:1 18:1	DOPE	-0.04±0.04	[143]

PE

Lipid	Acyl Chains	Matrix	c_0 (nm^{-1})	Source
POPE	16:0 18:1	-	-0.317±0.007	[144]
DiPoPE	16:1 16:1	-	-0.382±0.009	[144]
DOPE	18:1 18:1	-	-0.409±0.010	[144]

Table S2: List of membrane compositions simulated by CG-MD; the number of lipids for each type are shown.

System name	POPC	DOPC	POPE	DOPE	CDL1	CDL2	POPG	DOPG
1:Complex WT (CL-1)	648	2486	162	1460	648	0	0	0
2: Complex SFA2 (CL-1)	1406	1352	432	1568	648	0	0	0
3: Complex SFA3 (CL-1)	972	1406	1188	1188	648	0	0	0
4: Complex WT (CL-2)	648	2486	162	1460	0	648	0	0
5: Complex SFA2 (CL-2)	1406	1352	432	1568	0	648	0	0
6: Complex SFA3 (CL-2)	972	1406	1188	1188	0	648	0	0
7: Complex WT (PG)	540	2974	108	1188	0	0	324	270
8: Complex SFA2 (PG)	1080	1838	378	1352	0	0	648	108
9: Complex SFA3 (PG)	918	1406	1188	1134	0	0	648	108
10: Ideal DOPL (CL-1)	0	2704	0	1622	1080	0	0	0
11: Ideal POPL (CL-1)	2704	0	1622	0	1080	0	0	0
12: Ideal DOPL (CL-2)	0	2704	0	1622	0	1080	0	0
13: Ideal POPL (CL-2)	2704	0	1622	0	0	1080	0	0
14: Ideal DOPL (PG)	0	2704	0	1622	0	0	0	1080
15: Ideal POPL (PG)	2704	0	1622	0	0	0	0	1080
16: Outer IMM leaflet (CL-1)	594	2378	162	1406	864	0	0	0
17: Inner IMM leaflet (CL-1)	648	2594	162	1514	486	0	0	0
18: Outer IMM leaflet (CL-2)	594	2378	162	1406	0	864	0	0
19: Inner IMM leaflet (CL-2)	648	2594	162	1514	0	486	0	0
20: Pure CL-1	0	0	0	0	5408	0	0	0
21: Pure CL-2	0	0	0	0	0	5408	0	0

Table S3: Strains used in this study

Experimental Models: Organisms/strains

Reagent or Resource	Source	Description
W303a (*MATa leu2-3112 trp1-1 can1-100 ura3-1 ade2-1 his3-11,15*)	ATCC	Haploid background strain
W303a, *ole1::Pm1-OLE1*	This study	Weak constitutive promoter driving *OLE1* expression (SFA4)
W303a, *ole1::Pm2-OLE1*	This study	Weak constitutive promoter driving *OLE1* expression (SFA3)
W303a, *ole1::Pm3-OLE1*	This study	Medium strength constitutive promoter driving *OLE1* expression (SFA2)
W303a, *ole1::Pm4-OLE1*	This study	Strong constitutive promoter driving *OLE1* expression (SFA1)
W303a, *ole1::Pm1-OLE1* Δ*crd1*::KanMX6	This study	SFA4Δ*crd1*
W303a, *ole1::Pm2-OLE1* Δ*crd1*::KanMX6	This study	SFA3Δ*crd1*
W303a, *ole1::Pm3-OLE1* Δ*crd1*::KanMX6	This study	SFA2Δ*crd1*
W303a, *ole1::Pm4-OLE1* Δ*crd1*::KanMX6	This study	SFA1Δ*crd1*
W303a, Δ*crd1*::KanMX6	This study	
W303a, Δ*atp20*::His3	This study	
W303a, *ole1::Pm4-OLE1* Δ*atp20*::His3	This study	SFA1Δ*atp20*
W303a, *ole1::Pm3-OLE1* Δ*atp20*::His3	This study	SFA2Δ*atp20*
W303a, Δ*mgm1*::His3	This study	
W303a, Δ*mic60*::His3	This study	
W303a, *ole1::Pm4-OLE1* Δ*mic60*::His3	This study	SFA1Δ*mic60*
W303a, *ole1::Pm3-OLE1* Δ*mic60*::His3	This study	SFA2Δ*mic60*

Table S4: Plasmids used in this study

Plasmid	Source	Description
pPW1882	Dr. Peter Walter	Mitochondrial matrix RFP

pPW1409	Dr. Peter Walter	ER-localized RFP
pRS416	Dr. Arnold Seo	Vacuole Pho8 GFP
pSEC7-RFP	Dr. Arnold Seo	Early Golgi-RFP
Cox4-GFP	Dr. Zhiping Xie	CIV subunit 4 IMM localized-GFP

Table S5: Antibodies used in this study

Reagent or Resource	Source	Description
Anti-ATP synthase subunit β antibody	Dr. Alexander Tzagoloff	Goat, polyclonal[145]

Multimedia file captions

Movie S1: Animation depicting the mean curvature map within the IMM of a cristae-containing SFA2 mitochondrion.

Movie S2: Animation depicting the mean curvature map within the flat IMM of a SFA4 mitochondrion.

Movie S3: Animation depicting the mean curvature map within the IMM of an onion-like SFA4 mitochondrion.

Movie S4: Animation depicting the simulated distribution of ATP synthases (large red spheres), ANTs, ATP (small blue spheres) and ADP (small yellow spheres) within the IMM of a cristae-containing SFA2 mitochondrion.

Movie S5: Animation depicting the simulated distribution of ATP synthases (large red spheres), ANTs, ATP (small blue spheres) and ADP (small yellow spheres) within the IMMs of an onion-like SFA4 mitochondrion.

Movie S6: Animation showing the change in the shape of membrane for bending modulus 15 k_BT, with collar force 8 pN/nm, and D_0 fixed at 0.0175 nm^{-1}. The movie shows the shape as C_0 increases.

Movie S7: Animation showing the change in the shape of membrane for bending modulus 15 k_BT, with collar force 8 pN/nm, and C_0 fixed at 0.0225 nm^{-1}. The movie shows the shape as D_0 increases.

Experimental Procedures

Strains and growth media

The yeast strains used in this study can be found in Table S3. Yeast cells were grown in YPEG (1% Bacto yeast extract, 2% Bacto peptone, 2% Ethanol, 2.5% Glycerol), YPD medium (1% Bacto yeast extract, 2% Bacto peptone, 2% glucose) or complete supplement mixture (CSM, 0.5% Ammonium Sulfate, 0.17% yeast nitrogen base without amino acids and 2% glucose) lacking appropriate amino acids for selection. Yeast mutants were generated by PCR-based homologous recombination, ORFs of the gene of interest were replaced by either *KanMX* or *His3MX6* cassettes. For *OLE1* promoter substitution, a set of previously generated mutant *TEF1* promoters were utilized[146]. An additional, weaker promoter (*Pm1)* was generated by error prone PCR and added to this set. Promoter substitution was completed on the haploid base strain W303a as previously described[147].

Yeast physiology

Growth on non-fermentable carbon sources were assayed using growth curves on 24-well plates (Avantor) sealed with a gas permeable film (Diversified Biotech). Cells were first grown in biological triplicate overnight in complete synthetic medium (CSM) containing 2% glucose. Cells were back-diluted 1:100 in fresh CSM containing 2% glucose or 3% glycerol and shaken in a plate reader (Tecan) for 48 hours. Specific growth rates were extracted from the exponential phase of growth. For viability assays, cells were first grown in the same fashion as for yeast growth curves but were serially diluted onto CSM plates (1:5 successive dilutions) containing either 2% glucose or 3% glycerol and 2% ethanol. Plates were grown for 3 days on glucose plates, and for 4 days for ethanol/glycerol plates.

For microaerobic growth, cells were pre-incubated overnight in CSM without uracil (2% glucose) in a controlled temperature shaker at 30°C. Cells were then back diluted into fresh synthetic medium and grown to stationary phase in home-built microaerobic chambers with limited oxygen supply. Chambers consisted of glass culture tubes with tight fitting rubber caps; tubing allowed for gas efflux into an attached bubbler. Live cell imaging was conducted on aliquots, and cell pellets were resuspended in sterile water, lysed and flash frozen for lipidomics analysis.

Lipidomics

Lipid compositions of whole cells and isolated mitochondria from yeast strains were conducted at Lipotype GmbH (Dresden, Germany). Mass spectrometry-based lipid analysis was performed as previously described[148,149]. Lipids were extracted using a two-step chloroform/methanol procedure[148]. Samples were spiked with internal lipid standard mixture containing: CL 14:0/14:0/14:0/14:0, ceramide 18:1;2/17:0 (Cer), diacylglycerol 17:0/17:0 (DAG), lyso-phosphatidate 17:0 (LPA), lyso-phosphatidyl-choline 12:0 (LPC), lysophosphatidylethanolamine 17:1 (LPE), lyso-phosphatidylinositol 17:1 (LPI), lysophosphatidylserine 17:1 (LPS), phosphatidate 17:0/14:1 (PA), phosphatidylcholine 17:0/14:1 (PC), PE 17:0/14:1, PG 17:0/14:1, PI 17:0/14:1, phosphatidylserine 17:0/14:1 (PS), ergosterol ester 13:0 (EE) and triacylglycerol 17:0/17:0/17:0 (TAG). After extraction, the organic phase was transferred to an infusion plate and dried in a speed vacuum concentrator. 1st step dry extract was re-suspended in 7.5 mM ammonium acetate in chloroform/methanol/propanol (1:2:4, v:v:v) and 2nd step dry extract in 33% ethanol solution of methylamine in chloroform/methanol (0.003:5:1; v:v:v). All liquid handling steps were performed using Hamilton Robotics STARlet robotic platform with the Anti Droplet Control feature for organic solvents pipetting. Samples were analyzed by direct infusion on a QExactive mass spectrometer (Thermo Scientific)

equipped with a TriVersa NanoMate ion source (Advion Biosciences). Samples were analyzed in both positive and negative ion modes with a resolution of $R_{m/z=200}$=280000 for MS and $R_{m/z=200}$=17500 for MSMS experiments, in a single acquisition. MSMS was triggered by an inclusion list encompassing corresponding MS mass ranges scanned in 1 Da increments[150]. Both MS and MSMS data were combined to monitor EE, DAG and TAG ions as ammonium adducts; PC as an acetate adduct; and CL, PA, PE, PG, PI and PS as deprotonated anions. MS only was used to monitor LPA, LPE, LPI and LPS as deprotonated anions; Cer and LPC as acetate adducts. Data were analyzed with in-house developed lipid identification software based on LipidXplorer[151,152]. Data post-processing and normalization were performed using an in-house developed data management system. Only lipid identifications with a signal-to-noise ratio >5, and a signal intensity 5-fold higher than in corresponding blank samples were considered for further data analysis.

Mitochondria purification

Yeast mitochondria were isolated from 1L of yeast cells grown in YPEG (1% Bacto yeast extract, 2% Bacto peptone, 2% Ethanol, 3% Glycerol) or YPD medium (1% Bacto yeast extract, 2% Bacto peptone, 2% glucose) at 30°C as previously described[153,154]. Cells were grown to stationary phase and harvested in a buffer consisting of 100mM Tris/H_2SO_4 (pH 9.4) and 10mM dithiothreitol. Spheroplasts were formed from digestion of the cell wall using Zymolyase 20-T (MP Biomedicals) in a buffer containing 20mM Potassium Phosphate (pH 7.4) and 1.2M Sorbitol. Spheroplasts were lysed by homogenization using a glass homogenizer and subsequently centrifuged to remove unbroken cells, large debris and nuclei. Enriched mitochondria were pelleted and resuspended in SEM buffer (10mM MOPS/KOH (pH 7.2), 250mM Sucrose and 1mM EDTA), snap frozen and stored for up to 1 month at -80 °C. To obtain purified mitochondria, bereft of contamination from other organelles, such as microsomes, Golgi and vacuoles, the crude mitochondrial fraction is subjected to a sucrose density cushion ultracentrifugation. Cushions are poured containing 60% and 32% (w/v) sucrose concentrations in EM buffer (10mM MOPS/KOH (pH 7.2), 1mM EDTA). Density cushions containing crude mitochondrial samples in SEM buffer are subjected to ultracentrifugation in a SW32 Ti swinging-bucket rotor for 1 hour at 100,000 x g at 4 ºC. The yellow/brown band at the 60/32% (w/v) sucrose interface is removed and centrifuged to pellet purified mitochondria for subsequent analysis. Mitochondrial protein quantity was determined via BCA assay.

Mitoplasts containing an intact inner mitochondrial membrane stripped of the outer membrane were isolated as previously described[55]. After initial incubation of isolated mitochondria in a hypotonic buffer followed by centrifugation for 10 minutes at 14,000 x g at 4 ºC. Mitoplasts were resuspended in SEM buffer prior to lipidomic analysis.

Respirometry

Oxygen consumption rates (OCR) of whole cell yeast strains were measured with a Clark electrode (YSI 5300A Biological Oxygen Monitor System). Cells were grown in biological replicates overnight in CSM containing 0.4% glucose (starvation conditions). Cells were then back-diluted into fresh CSM and grown to OD 0.4-0.6. OCRs were quantified after initial stirring of culture for 3 minutes in a thermostatically controlled chamber at 30 °C. Respiration rates were determined after normalization to OD of the sample.

Live cell microscopy

To assess mitochondrial morphology, cells were initially grown in biological replicates overnight in CSM containing 0.4% glucose under selection conditions. Cells were then back diluted and imaged in an exponential phase. Prior to imaging, cells were plated on 8 well chambered coverglass (Nunc Lab-Tek, Thermo Fisher Scientific) pre-incubated with concanavalin A (MP Biomedicals). Live cell microscopy was conducted using Plan-Apochromat

63x/1.4 Oil DIC M27 on the Zeiss LSM 880 with Airyscan (default processing settings); image acquisition and processing were performed using ZEN software.

For image analysis, cells were split into 3 groups based on mitochondrial morphology: 'aberrant' groups display a punctate cluster at the center of the cell, whilst 'fragmented' groups display a lack of tubular morphology and consist of individual mitochondrial puncta separated within the cell (Figure S2B). Normal mitochondrial morphology is associated with tubes spanning the length of the cell that display regular lateral motion. Percentage 'mitochondrial abnormality' is derived from combining the amount of cells with an aberrant or fragmented morphology divided by the total number of cells. At least 50 cells were quantified in a given sample and replicates were of individually grown cultures. To visualize the yeast cell wall, cells were stained with calcofluor white (Sigma-Aldrich), which is able to bind chitin within the cell wall.

Membrane potential was assayed by imaging of cells stained with Tetramethylrhodamine, ethyl ester (TMRE, Thermo Fisher Scientific T669). Cells were first grown to exponential phase in CSM containing 0.4% glucose and stained with 200nM TMRE for 20 minutes. Cells were then washed twice with water prior to imaging on the Zeiss LSM 880 with Airyscan, using a 561 nm laser line with 1% laser power. For analysis of membrane potential in uncoupled conditions, cells were incubated with 20 μM carbonyl cyanide m-chlorophenyl hydrazone (CCCP, Sigma-Aldrich) for 10 minutes prior to incubation with TMRE. For analysis of membrane potential in ATP synthase inhibited conditions, cells were incubated with 5 μM oligomycin for 45 minutes prior to incubation with TMRE. Peak intensities were quantified from at least 10 cells in each condition.

Blue Native-PAGE analysis

Isolated mitochondria solubilized in digitonin (0.5:1 g/g protein) were assayed by BN-PAGE as previously described[155], with minor modifications. 200-400 μg of mitochondria were incubated with digitonin for 10 minutes prior to centrifugation at 20,000 x g for 30 mins at 4 ºC. The subsequent supernatant was mixed with native PAGE buffer and glycerol and loaded onto precast native PAGE gels (Invitrogen). ATP synthase dimerization state was probed using β-ATP synthase primary antibody (1:1000) and anti-rabbit IgG secondary antibody (Thermo Fisher Scientific).

Electron Microscopy

Blocks of late exponential phase yeast cells were prepared either by high-pressure freezing/freeze substitution (HPF-FS)[156] (SFA4, SFA2Δ*crd1*, Δ*atp20*,) or chemical fixation followed by partial cell wall digestion[157] (SFA2, SFA4, Δ*crd1* and microaerobic cells) as previously described. Cell wall digestion was required for high contrast staining of WT-like tubular CM for 3D segmentation. For microaerobic cells, chemical digestion was performed with 0.25 mg/mL zymolyase-20T for one hour at room temperature. Aerobically-grown mutant cells lacking CMs showed sufficient membrane contrast in HP-FS samples. Thin sections about 60 nm thick were cut from the blocks of yeast with a Leica ultramicrotome and placed on 200-mesh uncoated thin-bar copper grids. A Tecnai Spirit (FEI, Hillsboro, Oregon) electron microscope operated at 120 kV was used to record images with a Gatan Ultrascan 4K x 4K CCD camera at 6.0, 2.9, and 1.9 nm/pixel.

Tomography

Semi-thick sections of thickness about 300 nm were cut from the blocks of yeast with a Leica ultramicrotome and placed on 200-mesh uncoated thin-bar copper grids. 20-nm colloidal gold particles were deposited on each side of the grid to serve as fiducial cues. The specimens were irradiated for about 20 min to limit anisotropic specimen thinning during image collection at the magnification used to collect the tilt series before initiating a dual-axis tilt series. During data

collection, the illumination was held to near parallel beam conditions and the beam intensity was kept constant. Tilt series were captured using SerialEM (University of Colorado, Boulder) software on a Tecnai HiBase Titan (FEI) electron microscope operated at 300 kV and 0.81 nm/pixel. Images were recorded with a Gatan 4K x 4K CCD camera. Each dual-axis tilt series consisted of first collecting 121 images taken at 1 degree increment over a range of -60 to +60 degrees followed by rotating the grid 90 degrees and collecting another 121 images with the same tilt increment. To improve the signal-to-noise ratio, 2x binning was performed on each image by averaging a 2x2 x-y pixel box into 1 pixel using the newstack command in IMOD (University of Colorado, Boulder). The IMOD package was used for tilt-series alignment, reconstruction, and volume segmentation. R-weighted back projection was used to generate the reconstructions.

Mesh Generation and Analysis

3D *in silico* reconstructions of mitochondria were generated from electron-tomographic images. The software IMOD was used to trace the mitochondrial membranes in 2D: the outer leaflet of the OM, and the inner leaflet of the IBM and CM were manually traced as separate objects, following procedures previously described[7]. Subsequently, 2D traces were imported into Blender using the NeuropilTools module in CellBlender. The program Contour Tiler[158] — integrated with NeuropilTools — was used to generate 3D triangulated meshes in Blender. The triangulation was performed individually for each membrane object in each mitochondrion. Afterwards, the Boolean Difference Modifier was used to subtract the CM object from the IBM object, generating in this manner the CJs in the IBM. The meshes were refined with the Smooth and Normal Smooth improvement tools from GAMer2[91]. Curvature calculations were carried out with GAMer2, using the MDSB algorithm. For all curvature analysis, the smooth curvature after one iteration was considered. This smoothing represents the average curvature of a vertex and its neighbors. Surface areas and volumes were calculated using the CellBlender add-on in Blender.

Modeling Procedures

ATP production modeling

The computational for ATP generation in mitochondria is based on previous modeling efforts [97,159–162]. We solve the reactions (detailed below) using MCell [163] to accurately capture the stochastic nature of the events underlying ATP production in the small volumes of the mitochondria. The model has a total of 19 equations and 41 parameters and the thermodynamic details are given in [159]. We briefly describe the main components of the model below.

ATP synthase: The ATP synthase model is composed of ATP synthase (represented as E) that can be in six states (Figure S3F), representing different protein configurations. Each state corresponds with a number from 1 to 6, and each transition has associated a rate constant k_{ij} (transition from the state i → j). In some cases k_{ij} depends on the membrane potential, proton concentration, or phosphate concentration. The list of reactions and model parameters are given below, reproduced from[159]. The model was adapted from the work of Pietrobon and Caplan[164].

ATP synthase is modeled as a membrane protein that can transport protons (H^+) from and to the matrix and synthesize ATP. The translocation of 3 H^+ is coupled to the phosphorylation of one ADP into ATP, approximating the stoichiometry of the yeast ATP synthase with a c_{10} ring (10 H^+/ 3 ATP). The free enzyme with its negative charged cavity facing the IMS is represented by E^{-3}. Three protons can bind, generating the transition to state EH_3. The protons can be translocated to the matrix through the reaction ($EH_3 \rightarrow H_3E$) or $EH_3 \rightarrow H_3E^*$. A transition to state H_3ES can follow binding one ADP molecule from the matrix (represented as D_m) under constant phosphate (P_i) concentration, which is kept at 20 mM. This is followed by the production of one molecule of ATP (T_m) through the reaction $H_3ES \rightarrow H_3E + T_m$. Finally, in the transition $H^3E \rightarrow {}^{-3}E + 3H^+_m$ three protons are unbound in the matrix. The negative charged cavity of the enzyme can also transition from facing the matrix (state ${}^{-3}E$) to facing the IMS (state E^{-3}).

Transition 6 → 5 accounts for the binding of 3 protons from the IMS to the free enzyme (state 6, E^{-3}), two transitions can occur from here: transition 5 → 4 represents the transport of the protons to the matrix or transition 5 → 2 that represents the transport of the protons to the matrix without producing ATP. In state 4, ADP can bind to the enzyme (transition 4 → 3) and subsequently ATP can be synthesized (transition 3 → 2). This is followed by the unbinding of the protons in the matrix (transition 2 → 1), arriving at state 1.

List of Reactions for the ATP synthase model: (1) $^{-3}E + 3H^+_m \leftrightarrow H_3E$, k_{12}, k_{21} (2) $H_3E + T_m \leftrightarrow H_3ES$, k_{23}, k_{32} (3) $H_3ES \leftrightarrow H_3E^* + D_m$, k_{34}, k_{43} (4) $H_3E^* \leftrightarrow EH_3$, k_{45} , k_{54} (5) $EH_3 \leftrightarrow E^{-3} + H^+_i$, k_{56}, k_{65} (6)$E^{-3} \leftrightarrow {}^{-3}E$, k_{61}, k_{16}

Parameter values for the ATP synthase model: $k_{43} = 2\times10^6\ M^{-1}\ s^{-1}$, $k_{34} = 100\ s^{-1}$, $k_{12} = 25\ s^{-1}$, $k_{21} = 40\ s^{-1}$, $k_{65} = 3969\ s^{-1}$, $k_{56} = 1000\ s^{-1}$, $k_{61} = 33989\ s^{-1}$, $k_{16} = 146516\ s^{-1}$, $k_{54} = 1\times10^2\ s^{-1}$, $k_{45} = 100\ s^{-1}$, $k_{25} = 5.85\times10^{-30}\ s^{-1}$,$k_{52} = 1\times10^{-20}\ s^{-1}$, $k_{32} = 5\times10^3\ s^{-1}$, $k_{23} = 5\times10^6\ M^{-1}\ s^{-1}$

Modeled distribution of ATP synthases: The density of ATP synthases has been estimated at 3070 ATP synthases per um^2 in areas of high membrane curvature[165], this is consistent with ATP synthase densities estimated from yeast [166]. For each reconstruction, we calculated the surface area formed by vertices with first principal curvature higher than 70 μm^{-1}, and with this the number of ATP synthases was estimated for each organelle. For instance, the surface area of high curvature for the reconstruction of an SFA2 mitochondria is 0.144 μm^2, which leads to an

estimation of 433 units of ATP synthases in this reconstruction. To perform the spatial simulations, ATP synthases were distributed randomly in the regions of high curvature. For each mitochondrion, the total number of ATP synthases was kept the same.

ATP/ADP translocator (ANT) model: The model for the ATP/ADP translocator (ANT) is composed of 11 states and 22 chemical reactions, listed below. The kinetic diagram is presented in Figure S3F. The free protein is represented with the letter L in the diagram; it can bind ADP (D) or ATP (T) molecules from the matrix side (on the right) or IMS side (on the left), forming a triple molecular state. State TLD for instance represents a state with one ATP bound from the IMS and one ADP from the matrix side. The reaction that transports ATP from the matrix to the IMS is DLT → TLD, the rate constant for this reaction is k_p, the reverse reaction imports ATP to the matrix and exports ADP to the IMS, with rate constant k_{cp}. Futile translocations can also occur translocating one molecule of ATP by another ATP (TLT → TLT'). TLT and TLT' represent the same state, but they are differentiated to measure the rate of these translocations.

List of Reactions for the ANT model: (1) $T_m + L \leftrightarrow LT$, k^+_{Tm} , k^-_{Tm} (2) $D_m + L \leftrightarrow LD$, k^+_{Dm} , k^-_{Dm} (3) $T_i + L \leftrightarrow TL$, , k^+_{Ti} , k^-_{Ti} (4) $D_i + L \leftrightarrow DL$, k^+_{Di} , k^-_{Di} (5) $T_i + LT \leftrightarrow TLT$, k^+_{Ti} , k^-_{Ti} (6) $D_i + LT \leftrightarrow DLT$, k^+_{Di} , k^-_{Di} (7) $T_i + LD \leftrightarrow TLD$, k^+_{Ti} , k^-_{Ti} (8) $D_i + LD \leftrightarrow DLD$, k^+_{Di} , k^-_{Di} (9)TLD → DLT, k_{cp} (10) DLT → TLD, k_p (11) TLT → TLT', k_t (12) TLT' → TLT, k_t (13) DLD → DLD', k_d (14) DLD → DLD, k_d

Parameter values for the ANT model at Δϕ 180 mV: $k^-_{Tm} = 4\times10^4\ s^{-1}$, $k^+_{Tm} = 6.4\times10^6\ M^{-1}\ s^{-1}$, $k^-_{Ti} = 200\ s^{-1}$, $k^+_{Ti} = 4\times10^5\ M^{-1}\ s^{-1}$,$k^-_{Dm} = 4\times10^4\ s^{-1}$, $k^+_{Dm} = 4\times10^6\ M^{-1}\ s^{-1}$, $k^-_{Di} = 100\ s^{-1}$, $k^+_{Di} = 4\times10^6\ M^{-1}\ s^{-1}$, $k_p = 92\ s^{-1}$, $k_{cp} = 3.5\ s^{-1}$, $k_d = 4.8\ s^{-1}$, $k_t = 5.8\ s^{-1}$

Modeled distribution of ANTs: The density of ANTs has been estimated at 0.2 nm/mg protein in rat liver mitochondria[167]. Assuming that 1 nm/mg protein is approximately 1.25 mM[160] leads to a concentration of 0.25 mM. With this concentration, the number of ANTs in a given reconstruction can be estimated. Using the total mitochondrial volume proportionality with ANT concentration, we set the number of ANTs in SFA2 as 7678. In the onion mitochondrion, the number of ANTs were set at 7531. Thus, both types of mitochondria analyzed contained a 17:1 ratio of ANTs to ATP synthases.

VDAC model: To model the exit of ATP molecules to the cytosol we included VDACs, the main mechanism for metabolites to cross the OM. We implemented a simple model assuming VDAC proteins interact with ATP molecules and translocate them to the cytosol by the reaction VDAC + $ATP_{IMS} \rightleftharpoons$ VDAC + ATP_{cyto}. In all simulations, VDAC proteins were homogeneously distributed in the OMM. VDAC abundances were set as proportional to the total mitochondrial volume encapsulated by the OMM.

Parameters for the VDAC mode: rate constant of the reaction, $k_{vdac} = 1\times10^6\ M^{-1}\ s^{-1}$, the density of VDACs[168], δ = $1\times10^4\ \mu m^{-2}$, the number of VDACs considered in the simulations, N_{vdac} = 10268 for CM-containing SFA2 mitochondria and 4979 for onion-like SFA4 mitochondria.

Metabolite buffers: ATP and ADP molecules can interact with different cations, be bound, or ionized. The total concentration of ATP and ADP molecules can be distributed in several compounds like ATP^{4-}, ADP^{3-}, $ATPMg^{2-}$, etc. The final distributions can be estimated by coefficients representing the fraction of unbound ATP in the matrix or the IMS. For our model, mitochondrial ADP^{3-} and ATP^{4-} concentrations were estimated analogously to published data [160] as $[ADP]_{m,free} = 0.8\ [ADP]_m$, $[ATP]_{m,free} = [ATP]_m$, $[ATP^{4-}] = 0.05\ [ATP]_{free}$ and $[ADP^{-3}] = 0.45\ [ADP]_{free}$. The initial concentrations of ATP and ADP in the matrix were set to 13 mM and 2 mM,

respectively, and to 6.5 mM and 0.1 mM in the IMS and cytosol. In some simulations, these concentrations were kept constant.

Well-mixed model of ATP generation: A system of ordinary differential equations was derived from the reactions above (given in[159]) and used to calculate the rate of ATP generation in a well-mixed model, without considerations of mitochondrial geometry.

Molecular dynamics simulations

Coarse grained molecular dynamics models of systems with varying compositions were generated using insane.py[169] and Martini 2.2 force-field parameters[170,171]. Minimization and equilibration followed the conventional protocols established by CHARMM-GUI[172,173], summarized briefly here. Initial soft-core minimization is followed by steepest descent to generate an integrator ready relaxed configuration. The systems are jumped to 303 K by random assignment of velocities and the systems undergo several steps of NPT restrained equilibration. All equilibration steps were run with the Berendsen barostat[174]. Over the course of restrained equilibration stages, the timestep was gradually increased from 2 to 20 fs, and bilayer headgroup restraints were reduced from 200 to 20 KJ/mol nm^2. Systems are followed by several microseconds of NPT production using a semiisotropic Parinello-Rahman barostat[175]. All equilibration and production simulations use the Bussi-Donadio-Parinello velocity-rescaling thermostat[176] with reaction-field electrostatics and shifted Van der Waals potentials both with 1.1 nm cutoff[177]. Molecular dynamics simulations were run using gromacs 2022.1[178,179]. Force-field parameters, topologies, and simulation control parameters to reproduce this work are available https://github.com/RangamaniLabUCSD/2022-mitochondria-lipidomics-md. Henceforth all timescales reported are in simulation time, and not scaled using the conventional factor of 4 for Martini 2.2 simulations.

The bending modulus of the membrane for each composition was estimated by analyzing the height fluctuation spectra[74,76,80,180,181] of systems approximately 40 by 40 nm in size over 5 μs of production. Assuming the Helfrich Hamiltonian in the limit of small deformations (Monge gauge), zero membrane tension, and equipartition of energy, the power spectrum of the bilayer height fluctuations is given by,

$$< |h(\mathbf{q})|^2 > \; = \frac{k_B T}{L^2 K_c q^4},$$

Where q is the magnitude of wave-vector $\mathbf{q}$, $k_B T$ is the Boltzmann constant and temperature, L is the system length, and K_c is the membrane bending modulus. Quadrilateral meshes representing the surfaces of each leaflet are fit to the headgroup region (defined by the pointcloud of PO4 and GL0 beads) using piecewise cubic interpolation. The neutral surface of the bilayer was assumed to be the mean of the two surfaces. Computing the squared discrete fourier transform of the neutral surface, we obtained the 2D power spectrum of height fluctuations. The 2D power spectrum was converted into 1D for subsequent analysis by radially binning and averaging. Fitting the 1D power spectrum to the theoretical enables the estimation of the membrane bending modulus. Quantifying the error of the estimate is performed using parametric bootstrapping analysis following recommendations by Erguder and Deserno[181]. In brief, we have a sequence of mean squared amplitudes, $< |h(\mathbf{q})|^2 >$ for each q corresponding to each trajectory frame. To obtain a meaningful error we consider these as samples from a continuous trajectory with some potential correlation. Statistical block averaging enables us to estimate the autocorrelation time of the data and further a correlation corrected standard deviation. The standard error of the bending modulus is determined from using parametric bootstrapping to sample values of spectral power for large wavenumbers. These are subject to

a non-linear fit to obtain a distribution of K_c values for each system from which we obtain the standard deviation. Processing of the data for the analysis was performed using numpy[182], Scipy[183], MDAnalysis[183], and a modified curvature analysis framework[184] available from https://github.com/ctlee/membrane-curvature.

The local neighbor enrichment for each lipid type was investigated using MDAnalysis[183]. For each lipid, we count the numbers and types of each lipid within a 1.5 nm radius. The position of each lipid was either the sole PO4 or GL0 bead in the headgroup region. Normalizing by the number of frames and copy number of each lipid type produces the mean number of lipids of each type around a lipid of a given type; Comparing this value against the probability derived from random chance with no interactions given by the system composition, we obtain the deviation from random chance.

Using smaller systems of approximately 15 by 15 nm in length we computed the lateral pressure profiles for each composition. Each small system was equilibrated for 4 μs followed by 200 ns of production with positions and velocities written out every 5 ps in full numerical precision. The stresses for each frame by reprocessing using gmx-ls in gromacs 2016.3[185]. Contours for stress calculation were spaced approximately 1 nm in the X and Y directions (in-plane of the membrane) and 0.1 nm in the Z direction (normal to the membrane). The lateral pressure, $p(z)$, is given by $p(z) = \sigma_{ZZ} - (\sigma_{XX} + \sigma_{YY})/2$, where σ_{XX}, σ_{YY}, and σ_{ZZ} are the diagonal components of the stress tensor. The discrete lateral pressure profile was fit using a piecewise cubic interpolation and the bending moment, $K_c c_0 = \int_0^\infty zp(z)dz$, was evaluated using numerical integration of the interpolated function. Errors of values derived from and the lateral pressure profile were estimated by splitting the collected production frames into three non-overlapping chunks.

Continuum modeling of tubular cristae formation

Overview of the model: The mathematical derivations of this model can be found in extensive detail in[103]. Here, we provide a brief summary of the equations. The membrane is modeled as a thin elastic shell in mechanical equilibrium. Table 1 summarizes the symbols and notation; all nonscalar quantities are denoted by a bar overhead.

Table 1: Notation and list of symbols

Notation	Description	Unit
W	Free energy density of the membrane	pN/nm
κ	Bending modulus of the membrane	pN · nm
κ_d	Deviatoric modulus of the membrane	pN · nm
$\bar{n}$	Surface normal	1
$a_{\alpha\beta}$, $a^{\alpha\beta}$	Metric tensor and its contravariant	–
$b_{\alpha\beta}$, $b^{\alpha\beta}$	Curvature tensor and its contravariant	–
$\bar{T}$	Surface traction	pN/nm
s	Arclength along the membrane	nm
ψ	Angle made by surface tangent with the horizontal direction	1
H	Mean curvature	nm^{-1}
D	Deviatoric curvature	nm^{-1}
C_0	Spontaneous mean curvature	nm^{-1}
D_0	Spontaneous deviatoric curvature	nm^{-1}

f^{α}	Tangential component of the force per unit area	pN/nm^2
f_n	Normal component of the force per unit area	pN/nm^2
λ	Membrane tension	pN/nm
λ_0	Tension at boundary	pN/nm
F_n	Traction at the boundary	pN/nm

The force balance on the membrane is given by

$$\overline{T}^{\alpha}_{;\alpha} + p\,\overline{n} + \overline{f} = 0 \qquad \text{(S1)}$$

where, $\overline{f} = f^{\alpha}\overline{a}_{\alpha} + f^{n}\overline{n}$ is the external force density applied to the membrane, p is normal pressure on the membrane and $\bar{T}$ is traction on the membrane and given by,

$$\overline{T}^{\alpha} = N^{\beta\alpha}\overline{a}_{\beta} + S^{\alpha}\overline{n} \qquad \text{(S2)}$$

Here, $\bar{N}$ in-plane components of the stress and is given by

$$N^{\beta\alpha} = \zeta^{\beta\alpha} + b^{\beta}_{\mu}M^{\mu\alpha} \text{ and } S^{\alpha} = -M^{\alpha\beta}_{;\beta} \qquad \text{(S3)}$$

where, $\zeta^{\beta\alpha}$ and $M^{\beta\alpha}$ are obtained from the following constitutive relationships [186]

$$\zeta^{\beta\alpha} = \rho\left(\frac{\partial F}{\partial a_{\alpha\beta}} + \frac{\partial F}{\partial a_{\beta\alpha}}\right) \text{ and } M^{\beta\alpha} = \rho\left(\frac{\partial F}{\partial b_{\alpha\beta}} + \frac{\partial F}{\partial b_{\beta\alpha}}\right), \qquad \text{(S4)}$$

with $F = W/\rho$ is the energy mass density of the membrane. Combining these we get the balance equations in tangent and normal direction

$$N^{\beta\alpha} - S^{\alpha}b^{\beta}_{\alpha} + f^{\alpha} = 0, \quad S^{\alpha}_{;\alpha} + N^{\beta\alpha}b_{\beta\alpha} + p + f_n = 0 \qquad \text{(S5)}$$

Here f^{α} and f_n are the tangential and normal components of external force applied to the membrane per unit area.

The energy density of the membrane W is taken as follows to account for the mean and the deviatoric curvature

$$W = \kappa(H - C_0)^2 + \kappa_d(D - D_0)^2. \qquad \text{(S6)}$$

To obtain tubular shapes, recasting the Helfrich energy in terms of the isotropic spontaneous curvature C_0 and the anisotropic spontaneous curvature D_0, is a commonly used approach[103,187–189]. In this case, the energy is written in terms of the mean curvature and the deviatoric curvature D. The deviatoric curvature is defined as half of the difference between the two principal curvatures.

The tangential force balance relation in Equation (S5)$_I$ simplifies as

$$\lambda' = 2\kappa(H - C0)C' + 2\kappa_d(D - D0)D_0' - f^s. \qquad \text{(S7)}$$

The normal force balance relation S5$_{II}$ (the shape equation) becomes

$$p = \frac{L'}{r} + W_H(2H^2 - K) - 2H(W + \lambda - W_D D) - f_n \quad , \qquad \text{(S8)}$$

where L relates to the expression of the traction, given by

$$\frac{L}{r} = \frac{1}{2}\left(W_H' - W_D'\right) - \frac{\cos\psi}{r} W_D = - F_n. \quad \text{(S9)}$$

where F_n is the traction acting normal to the membrane. The above relation gives a natural boundary condition for *L* at both the boundaries. At the center, it directly correlates with the value of pulling force as

$$p_f = \lim_{r \to 0} 2\pi r F_n = - 2\pi L(0). \quad \text{(S10)}$$

Area parameterization: The governing equations are solved in a patch of the membrane with fixed surface area, where the coat area of protein is prescribed. The arclength parametrization poses some difficulties since the total arclength varies depending on the equilibrium shape of the membrane. Therefore, we did a coordinate transformation of arclength to a local area *a* as given by

$$\frac{\partial}{\partial s} = 2\pi r \frac{\partial}{\partial a} \quad \text{(S11)}$$

Note that in the differential form, local area relates as $da = 2\pi r\, ds$

The tangential force balance relation in Equation S7 transforms to

$$\frac{\partial \lambda}{\partial a} = 2\kappa (H - C0) \frac{\partial C_0}{\partial a} + 2\kappa_d (D - D0) \frac{\partial D_0}{\partial a} - \frac{f^s}{2\pi r}. \quad \text{(S12)}$$

The normal force balance relation in Equation S8 becomes

$$p = 2\pi \frac{\partial L}{\partial a} + 2\kappa(H - C_0)(2H^2 - K) - 2H(W + \lambda - 2\kappa_d D(D - D_0)) - f_n \quad \text{(S13)}$$

where

$$\frac{L}{r} = \frac{\partial}{\partial a}\left(\kappa(H - C_0) - \kappa_d(D - D_0)\right) - \kappa_D (D - D_0)\frac{\cos\psi}{r}. \quad \text{(S14)}$$

Numerical methods: We solved the system of equations (Equation S11 to Equation S14) numerically to get the equilibrium shape of the membrane for a coat of protein at the center of an axisymmetric area patch. The solution domain is presented in Figure S5A, along with the input protein coat and the boundary conditions shown in Figure S5A. The protein coat includes both the spontaneous mean curvature cap and a combination of mean and deviatoric spontaneous curvature in the rest of the coat region (Figure S5B). Note that we introduced a shape variable ψ, which denotes the angle made by the tangent from its radial plane. The membrane is clamped at the domain boundary, where both the displacement and the angle $\psi = 0$. The membrane tension is also prescribed at the boundary. At the pole, ψ is taken to be zero, which indicates the smoothness at the center of the membrane. L is set to zero, indicating that there is no pulling force acting at the center.

To solve the system of equations, we used MATLAB-based bvp4c, a finite difference-based ODE solver with fourth-order accuracy (MATLAB codes are available https://github.com/Rangamani-lab/arijit_deviatoric_tube.2022). We used a nonuniform grid ranging from 1000 to 10000 points, with the finer grid towards the center. We used a large domain size of 10^6 nm^2 to avoid boundary effects but we show the results focusing on the membrane deformation (region enclosed by the dashed line in Figure S5C). The values of the different parameters used are given in the table

below.

List of parameters used in the simulations

Notation	Description	Range
C_0	Spontaneous mean curvature	0.01–0.035 nm^{-1}
D_0	Spontaneous deviatoric curvature	0–0.035 nm^{-1}
$\kappa = (\kappa_d)$	Bending modulus of the membrane	10-20 $k_B T$
a_{coat}	Coat area of protein	1.413×10^4 nm^2
a_{mem}	Total area of the membrane	5.65×10^5 nm^2
λ_0	Tension at boundary	0.01 pN/nm

Parameter ranges: The parameter ranges for the continuum model were chosen from the literature and from the CGMD simulations. The range of anisotropic spontaneous curvature induced by the ATP synthases was estimated from the CGMD simulations presented in[23] for a single ATP synthase dimer by estimating the two principal curvatures for the small deformation seen in Figure 1 of that work. Note that these estimates are obtained from digitizing the images and do not contain the information carried in the thermal fluctuations. The bending moduli range was in the range consistent with CG-MD calculations and previous experimental measurements. The tension and the coat area are free parameters in the model and were tuned such that we could obtain tubules of length and radius consistent with experimental measurements as shown in Figure 5B.

References

140. Symons, J.L., Cho, K.-J., Chang, J.T., Du, G., Waxham, M.N., Hancock, J.F., Levental, I., and Levental, K.R. (2021). Lipidomic atlas of mammalian cell membranes reveals hierarchical variation induced by culture conditions, subcellular membranes, and cell lineages. Soft Matter *17*, 288–297.

141. Kucerka, N., Tristram-Nagle, S., and Nagle, J.F. (2005). Structure of fully hydrated fluid phase lipid bilayers with monounsaturated chains. J. Membr. Biol. *208*, 193–202.

142. Jablin, M.S., Akabori, K., and Nagle, J.F. (2014). Experimental support for tilt-dependent theory of biomembrane mechanics. Phys. Rev. Lett. *113*, 248102.

143. Kaltenegger, M., Kremser, J., Frewein, M.P.K., Ziherl, P., Bonthuis, D.J., and Pabst, G. (2021). Intrinsic lipid curvatures of mammalian plasma membrane outer leaflet lipids and ceramides. Biochim. Biophys. Acta Biomembr. *1863*, 183709.

144. Frewein, M.P.K., Rumetshofer, M., and Pabst, G. (2019). Global small-angle scattering data analysis of inverted hexagonal phases. J. Appl. Crystallogr. *52*, 403–414.

145. Rak, M., and Tzagoloff, A. (2009). F1-dependent translation of mitochondrially encoded Atp6p and Atp8p subunits of yeast ATP synthase. Proc. Natl. Acad. Sci. U. S. A. *106*, 18509–18514.

146. Alper, H., Fischer, C., Nevoigt, E., and Stephanopoulos, G. (2005). Tuning genetic control through promoter engineering. Proceedings of the National Academy of Sciences *102*, 12678–12683. 10.1073/pnas.0504604102.

147. Degreif, D., de Rond, T., Bertl, A., Keasling, J.D., and Budin, I. (2017). Lipid engineering reveals regulatory roles for membrane fluidity in yeast flocculation and oxygen-limited growth. Metab. Eng. *41*, 46–56.

148. Ejsing, C.S., Sampaio, J.L., Surendranath, V., Duchoslav, E., Ekroos, K., Klemm, R.W., Simons, K., and Shevchenko, A. (2009). Global analysis of the yeast lipidome by quantitative shotgun mass spectrometry. Proceedings of the National Academy of Sciences *106*, 2136–2141. 10.1073/pnas.0811700106.

149. Klose, C., Surma, M.A., Gerl, M.J., Meyenhofer, F., Shevchenko, A., and Simons, K. (2012). Flexibility of a Eukaryotic Lipidome – Insights from Yeast Lipidomics. PLoS ONE *7*, e35063. 10.1371/journal.pone.0035063.

150. Surma, M.A., Herzog, R., Vasilj, A., Klose, C., Christinat, N., Morin-Rivron, D., Simons, K., Masoodi, M., and Sampaio, J.L. (2015). An automated shotgun lipidomics platform for high throughput, comprehensive, and quantitative analysis of blood plasma intact lipids. European Journal of Lipid Science and Technology *117*, 1540–1549. 10.1002/ejlt.201500145.

151. Herzog, R., Schwudke, D., Schuhmann, K., Sampaio, J.L., Bornstein, S.R., Schroeder, M., and Shevchenko, A. (2011). A novel informatics concept for high-throughput shotgun lipidomics based on the molecular fragmentation query language. Genome Biol. *12*, R8.

152. Herzog, R., Schuhmann, K., Schwudke, D., Sampaio, J.L., Bornstein, S.R., Schroeder, M., and Shevchenko, A. (2012). LipidXplorer: a software for consensual cross-platform lipidomics.

PLoS One *7*, e29851.

153. Gregg, C., Kyryakov, P., and Titorenko, V.I. (2009). Purification of Mitochondria from Yeast Cells. Journal of Visualized Experiments. 10.3791/1417.

154. Meisinger, C., Pfanner, N., and Truscott, K.N. Isolation of Yeast Mitochondria. Yeast Protocols, 033–040. 10.1385/1-59259-958-3:033.

155. Timón-Gómez, A., Pérez-Pérez, R., Nyvltova, E., Ugalde, C., Fontanesi, F., and Barrientos, A. (2020). Protocol for the Analysis of Yeast and Human Mitochondrial Respiratory Chain Complexes and Supercomplexes by Blue Native Electrophoresis. STAR Protoc *1*. 10.1016/j.xpro.2020.100089.

156. McDonald, K., and Müller-Reichert, T. (2002). Cryomethods for thin section electron microscopy. Methods Enzymol. *351*, 96–123.

157. Bauer, C., Herzog, V., and Bauer, M.F. (2001). Improved Technique for Electron Microscope Visualization of Yeast Membrane Structure. Microsc. Microanal. *7*, 530–534.

158. Edwards, J., Daniel, E., Kinney, J., Bartol, T., Sejnowski, T., Johnston, D., Harris, K., and Bajaj, C. (2014). VolRoverN: enhancing surface and volumetric reconstruction for realistic dynamical simulation of cellular and subcellular function. Neuroinformatics *12*, 277–289.

159. Garcia, G.C., Bartol, T.M., and Sejnowski, T.J. (2022). A Thermodynamically-Consistent Model for ATP Production in Mitochondria. bioRxiv, 2022.08.16.500715. 10.1101/2022.08.16.500715.

160. Magnus, G., and Keizer, J. (1997). Minimal model of beta-cell mitochondrial Ca2+ handling. Am. J. Physiol. *273*, C717–C733.

161. Bertram, R., Gram Pedersen, M., Luciani, D.S., and Sherman, A. (2006). A simplified model for mitochondrial ATP production. J. Theor. Biol. *243*, 575–586.

162. Saa, A., and Siqueira, K.M. (2013). Modeling the ATP production in mitochondria. Bull. Math. Biol. *75*, 1636–1651.

163. Kerr, R.A., Bartol, T.M., Kaminsky, B., Dittrich, M., Chang, J.-C.J., Baden, S.B., Sejnowski, T.J., and Stiles, J.R. (2008). Fast Monte Carlo Simulation Methods for Biological Reaction-Diffusion Systems in Solution and on Surfaces. SIAM J. Sci. Comput. *30*, 3126–3149.

164. Pietrobon, D., and Caplan, S.R. (1985). Flow-force relationships for a six-state proton pump model: intrinsic uncoupling, kinetic equivalence of input and output forces, and domain of approximate linearity. Biochemistry *24*, 5764–5776.

165. Acehan, D., Malhotra, A., Xu, Y., Ren, M., Stokes, D.L., and Schlame, M. (2011). Cardiolipin affects the supramolecular organization of ATP synthase in mitochondria. Biophys. J. *100*, 2184–2192.

166. Davies, K.M., Anselmi, C., Wittig, I., Faraldo-Gómez, J.D., and Kühlbrandt, W. (2012). Structure of the yeast F1Fo-ATP synthase dimer and its role in shaping the mitochondrial cristae. Proc. Natl. Acad. Sci. U. S. A. *109*, 13602–13607.

167. Forman, N.G., and Wilson, D.F. (1983). Dependence of mitochondrial oxidative phosphorylation on activity of the adenine nucleotide translocase. J. Biol. Chem. *258*, 8649–8655.

168. De Pinto, V., Ludwig, O., Krause, J., Benz, R., and Palmieri, F. (1987). Porin pores of mitochondrial outer membranes from high and low eukaryotic cells: biochemical and biophysical characterization. Biochim. Biophys. Acta *894*, 109–119.

169. Wassenaar, T.A., Ingólfsson, H.I., Böckmann, R.A., Tieleman, D.P., and Marrink, S.J. (2015). Computational Lipidomics with insane: A Versatile Tool for Generating Custom Membranes for Molecular Simulations. J. Chem. Theory Comput. *11*, 2144–2155.

170. Marrink, S.J., Risselada, H.J., Yefimov, S., Tieleman, D.P., and de Vries, A.H. (2007). The MARTINI force field: coarse grained model for biomolecular simulations. J. Phys. Chem. B *111*, 7812–7824.

171. Marrink, S.J., de Vries, A.H., and Mark, A.E. (2004). Coarse Grained Model for Semiquantitative Lipid Simulations. J. Phys. Chem. B *108*, 750–760.

172. Qi, Y., Ingólfsson, H.I., Cheng, X., Lee, J., Marrink, S.J., and Im, W. (2015). CHARMM-GUI Martini Maker for Coarse-Grained Simulations with the Martini Force Field. J. Chem. Theory Comput. *11*, 4486–4494.

173. Jo, S., Kim, T., and Im, W. (2007). Automated builder and database of protein/membrane complexes for molecular dynamics simulations. PLoS One *2*, e880.

174. Berendsen, H.J.C., Postma, J.P.M., van Gunsteren, W.F., DiNola, A., and Haak, J.R. (1984). Molecular dynamics with coupling to an external bath. J. Chem. Phys. *81*, 3684–3690.

175. Parrinello, M., and Rahman, A. (1981). Polymorphic transitions in single crystals: A new molecular dynamics method. J. Appl. Phys. *52*, 7182–7190.

176. Bussi, G., Donadio, D., and Parrinello, M. (2007). Canonical sampling through velocity rescaling. J. Chem. Phys. *126*, 014101.

177. de Jong, D.H., Baoukina, S., Ingólfsson, H.I., and Marrink, S.J. (2016). Martini straight: Boosting performance using a shorter cutoff and GPUs. Comput. Phys. Commun. *199*, 1–7.

178. Bauer, P., Hess, B., and Lindahl, E. (2022). GROMACS 2022.1 Source code 10.5281/zenodo.6451564.

179. Abraham, M.J., Murtola, T., Schulz, R., Páll, S., Smith, J.C., Hess, B., and Lindahl, E. (2015). GROMACS: High performance molecular simulations through multi-level parallelism from laptops to supercomputers. SoftwareX *1-2*, 19–25.

180. Brown, F.L.H. (2008). Elastic modeling of biomembranes and lipid bilayers. Annu. Rev. Phys. Chem. *59*, 685–712.

181. Ergüder, M.F., and Deserno, M. (2021). Identifying systematic errors in a power spectral analysis of simulated lipid membranes. J. Chem. Phys. *154*, 214103.

182. Harris, C.R., Millman, K.J., van der Walt, S.J., Gommers, R., Virtanen, P., Cournapeau, D.,

Wieser, E., Taylor, J., Berg, S., Smith, N.J., et al. (2020). Array programming with NumPy. Nature *585*, 357–362.

183. Virtanen, P., Gommers, R., Oliphant, T.E., Haberland, M., Reddy, T., Cournapeau, D., Burovski, E., Peterson, P., Weckesser, W., Bright, J., et al. (2020). SciPy 1.0: fundamental algorithms for scientific computing in Python. Nat. Methods *17*, 261–272.

184. E., B.-O. (2021). MDAnalysis Membrane Curvature Tool 10.5281/zenodo.5553452.

185. Vanegas, J.M., Torres-Sánchez, A., and Arroyo, M. (2014). Importance of Force Decomposition for Local Stress Calculations in Biomembrane Molecular Simulations. J. Chem. Theory Comput. *10*, 691–702.

186. Steigmann, D.J. (2018). Mechanics and Physics of Lipid Bilayers. In The Role of Mechanics in the Study of Lipid Bilayers, D. J. Steigmann, ed. (Springer International Publishing), pp. 1–61.

187. Kralj-Iglič, V., Pocsfalvi, G., Mesarec, L., Šuštar, V., Hägerstrand, H., and Iglič, A. (2020). Minimizing isotropic and deviatoric membrane energy - An unifying formation mechanism of different cellular membrane nanovesicle types. PLoS One *15*, e0244796.

188. Kabaso, D., Bobrovska, N., Gozdz, W., Gov, N., Kralj-Iglic, V., Veranic, P., and Iglic, A. (2012). On the role of membrane anisotropy and BAR proteins in the stability of tubular membrane structures. J. Biomech. *45*, 231–238.

189. Noguchi, H., Tozzi, C., and Arroyo, M. (2022). Binding of anisotropic curvature-inducing proteins onto membrane tubes. arXiv [cond-mat.soft].